

## Optomechanical Generation of Coherent GHz Vibrations in a Phononic Waveguide

Guilhem Madiot<sup>1,\*</sup>, Ryan C. Ng<sup>1,\*†</sup>, Guillermo Arregui<sup>1,2</sup>, Omar Florez<sup>1,3</sup>, Marcus Albrechtsen<sup>1,2</sup>, Søren Stobbe<sup>2,4</sup>, Pedro D. García<sup>1,‡</sup> and Clivia M. Sotomayor-Torres<sup>1,5</sup>

<sup>1</sup>*Catalan Institute of Nanoscience and Nanotechnology (ICN2), Campus UAB, Bellaterra, 08193 Barcelona, Spain*

<sup>2</sup>*DTU Electro, Department of Electrical and Photonics Engineering, Technical University of Denmark, Ørstedes Plads 343, DK-2800 Kgs. Lyngby, Denmark*

<sup>3</sup>*Dept. de Física, Universitat Autònoma de Barcelona, 08193 Bellaterra, Spain*

<sup>4</sup>*NanoPhoton—Center for Nanophotonics, Technical University of Denmark, Ørstedes Plads 345A, DK-2800 Kgs. Lyngby, Denmark*

<sup>5</sup>*ICREA—Institució Catalana de Recerca i Estudis Avançats, 08010 Barcelona, Spain*

 (Received 15 June 2022; revised 17 December 2022; accepted 27 January 2023; published 6 March 2023)

Nanophononics has the potential for information transfer, in an analogous manner to its photonic and electronic counterparts. The adoption of phononic systems has been limited, due to difficulties associated with the generation, manipulation, and detection of phonons, especially at GHz frequencies. Existing techniques often require piezoelectric materials with an external radiofrequency excitation that are not readily integrated into existing CMOS infrastructures, while nonpiezoelectric demonstrations have been inefficient. In this Letter, we explore the optomechanical generation of coherent phonons in a suspended 2D silicon phononic crystal cavity with a guided mode around 6.8 GHz. By incorporating an air-slot into this cavity, we turn the phononic waveguide into an optomechanical platform that exploits localized photonic modes resulting from inherent fabrication imperfections for the transduction of mechanics. Such a platform exhibits very fine control of phonons using light, and is capable of coherent self-sustained phonon generation around 6.8 GHz, operating at room temperature. The ability to generate high frequency coherent mechanical vibrations within such a simple 2D CMOS-compatible system could be a first step towards the development of sources in phononic circuitry and the coherent manipulation of other solid-state properties.

DOI: [10.1103/PhysRevLett.130.106903](https://doi.org/10.1103/PhysRevLett.130.106903)

Phononics has received less attention relative to its photonic and electronic counterparts, largely due to challenges associated with generating, transporting, manipulating, and detecting phonons, despite their potential as carriers of information signals [1–5]. Phononics is able to operate in the MHz and GHz regimes, connecting the frequency regimes of electronics and optics [6–8]. Analogously to photonic crystals, the dispersion relation of acoustic phonons can be engineered via structures with periodic elastic properties. In planar structures, careful design and nanofabrication have enabled the realization of mechanical band gaps in phononic crystals up to the GHz frequency range [9,10] and of phonon waveguiding via the introduction of linear defects into these crystals [11–13]. However, the excitation of phonons in such phononic circuits remains a challenge, with existing approaches relying on electromechanical actuation in piezoelectric materials [14–21]. While such an approach offers the technical advantages of ultracompact on-chip integrability with low power consumption, piezoelectric solutions are lacking in their ability to control and manipulate phonons and are restricted to a limited bandwidth often set by the specific interdigitated transducer design used for excitation. Alternatively, cavity optomechanical platforms

can finely control the phonon signal via radiation pressure forces while relying on an integrated photonic circuit rather than an external rf source, circumventing these aforementioned problems. Within these platforms, mechanical self-sustained oscillations driven by light, known as “phonon lasing” [22–26], can potentially be used to generate a phonon signal directly within a phononic circuit. This is typically achieved by side coupling an optomechanical cavity to another phononic waveguide and requires proper matching of the respective mechanical bandwidths and mode profiles [5,19,27,28]. A solution free of interdigitated transducers or more elaborate optomechanical architectures is thus an important building block for phononic circuitry.

Here, we present a 2D silicon phononic crystal (PnC) waveguide sustaining an acoustic guided mode around 6.8 GHz and exploit optomechanical interactions to transduce and generate coherent acoustic phonons directly within the phononic waveguide at room temperature. To realize this, an optomechanical interface is obtained by bringing together two identical PnC cavities separated by a slot photonic waveguide. The slot allows for light to be confined into disorder-induced localized cavities that strongly interact with the mechanics and enable optomechanical readout and amplification. Confinement of the

mechanical waveguide modes induced by reflections at the waveguide ends result in acoustic Fabry-Pérot fringes, with the associated strong optomechanical interaction leading to dynamical back-action and subsequent self-sustained oscillations (SSO) of certain mechanical modes. From a device perspective, the ability to coherently generate phonons in a 2D PnC waveguide cavity is a crucial step towards phonon launching into phononic circuitry.

We design a PnC waveguide in a 220 nm silicon membrane with etched *shamrock*-shaped holes [29] tiled in a triangular lattice, schematically illustrated in Fig. 1(a). The shamrocks are three overlapping elliptical holes, with each ellipse defined by short and long axes given by  $n_a = 0.23a_c$  and  $n_b = 0.30a_c$ , respectively, where  $a_c = 500$  nm is the PnC lattice period. This results in large islands of mass connected by very narrow necks which act as springs, which, consequently, opens a large phononic band gap centered around 6.2 GHz, enabling the creation of guided modes through line defects [13]. We achieve this by terminating a crystal with a straight free surface, indicated in red in Fig. 1(a), resulting in an acoustic waveguide that is a silicon “wire” with edges defined by air and by the shamrock PnC [27]. Additional details regarding the geometry are found in the Supplemental Material [30]. We calculate the waveguide band structures using finite-element-method (FEM) simulations and show two examples in Fig. 1(b). Each band is associated to  $z$ -symmetric or  $z$ -antisymmetric modes (with respect to the center mid-plane), shown in blue and red, respectively. Because of the optomechanical transduction described later, we focus only

on the former. The waveguide possesses a single propagating  $z$ -symmetric guided mode (thick blue line) for two geometries with horizontal pitches,  $a_c = 500$  (light blue border) and  $a_s = 560$  nm (yellow border), both with the same shamrock dimensions. The parameters are chosen to flatten the band of interest at the Brillouin zone edge and shift it away from the band gap edge to prevent coupling to bulk modes.

We explore the phononic waveguide with band structure given in Fig. 1(b) (left), where both the horizontal and vertical pitch coincide. To improve temporal confinement of the supported modes, we discretize the waveguide spectrum by creating a long acoustic cavity in the direction of the waveguide ( $x$ ). This cavity is formed by sandwiching a center region between two shield regions with horizontal pitches of  $a_c$  (blue) and  $a_s$  (yellow), respectively, schematically illustrated in Fig. 1(c). While both regions possess a guided mechanical mode [Fig. 1(b)], the greater horizontal period of the shield shifts it to a lower frequency and prevents coupling between the modes of each region. This results in an acoustic Fabry-Pérot cavity, significantly increasing the mechanical quality factor,  $Q_m$ , of the acoustic phonons [31]. We study structures with varying center region lengths  $L$ , while the shield region is set to have 8 unit cells along the  $x$  direction in all cases. Figure 1(d) shows the reconstructed waveguide band obtained after Fourier-transforming the  $y$  displacement along the free surface for the modes supported by a structure of length  $L = 20a_c$ , where all modes are shown with an identical mechanical  $Q$  factor of  $Q_m = 1200$ , a representative value

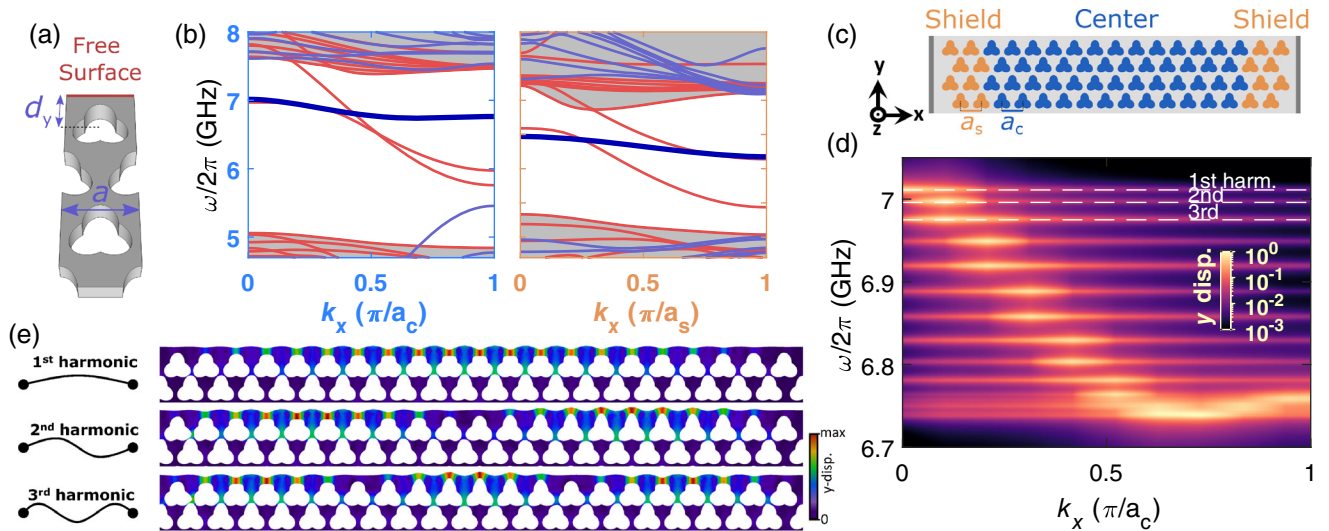


FIG. 1. (a) Supercell of the waveguide geometry with a silicon-air interface free boundary (red). (b) Mechanical band structure for the center (blue border) and shield (yellow border) regions showing the symmetric (blue) and antisymmetric (red) modes. (c) Schematic illustration of the phononic waveguide incorporating a center cavity region ( $n_a = 0.23a_c$ ,  $n_b = 0.30a_c$ ,  $a_c = 500$  nm) and shield region with larger period along the  $x$  direction ( $a_s = 560$  nm) to confine the mechanical mode. Schematic is not to scale. (d)  $y$  displacement spectrum as a function of the  $k$  vector. This simulation accounts for the full structure including the center and shield within one simulation, allowing observation of the acoustic Fabry-Pérot fringes. (e) Displacement mode profiles for the full structure showing acoustic confinement within the center region for the first three harmonics.

taken from experiment, while the different acoustic fringes are all expected to possess comparable linewidths [32]. The shield structure effectively generates a long cavity that inherits the dispersion properties of the underlying guided mode in the center region [Fig. 1(b), left]. This is also observed when the mode profiles are explored in real space, shown via the first three harmonics in Fig. 1(e), where the color scale indicates the  $y$  displacement. Along the waveguide axis, the modes have an increasing number of nodes and anti-nodes, mimicking a doubly clamped string. Unlike the simulations shown in Figs. 1(d) and 1(e), a real waveguide is subject to fabrication imperfections such as sidewall roughness which transforms the spectrospatial acoustic properties in the slow sound region (around the  $\Gamma$  point) when the length of the waveguide surpasses the acoustic localization length [33]. While this disorder is exploited in the optical domain in the following section, experimentally distinguishing between Fabry-Pérot cavity modes and disorder-induced mode localization is a complicated task beyond the present scope.

The shamrock crystal also supports a photonic band gap [34]. While the acoustic design sustains the guided mechanical mode of interest at a silicon-air free surface, this free surface is an inconvenient location for a photonic waveguide mode as that same interface does not provide efficient optical confinement, especially in terms of exhibiting radiation pressure along the slot walls, complicating the direct optomechanical transduction of motion. We exploit this otherwise disadvantageous nature of the mechanical waveguide by adding a mirror-symmetric version of the waveguide a distance 40 nm away from the original, which leads to two independent mechanical membranes separated by a center air-slot region, inside which a TE-like optical mode can be confined. The resulting design is shown in a false-color SEM image [Fig. 2(a)]. This slot photonic-crystal waveguide allows the electromagnetic field to be locally enhanced in the slot while guiding light along its length, creating a cavity-optomechanical system [35]. FEM simulations of the electromagnetic energy density in both a perfect and disordered slot are shown in Fig. 2(a) (see Supplemental Material [30] for associated photonic band structure and additional slot-guided mode details).

The suspended structures are fabricated in a silicon-on-insulator substrate (see Supplemental Material [30] with Refs. [36–38]). The resulting devices are optically characterized with a tapered fiber loop placed in contact along the waveguide axis, allowing light to evanescently couple into resonant optical modes of the structure [31]. A representative optical spectrum, normalized by the off-resonant transmission, is taken along a waveguide of length  $L_{\text{total}} \sim 84 \mu\text{m}$  and shown in the top panel of Fig. 2(b), where resonant optical modes manifest as spectral transmission dips. To understand the spatial structure of the observed optical modes, we acquire transmission spectra at

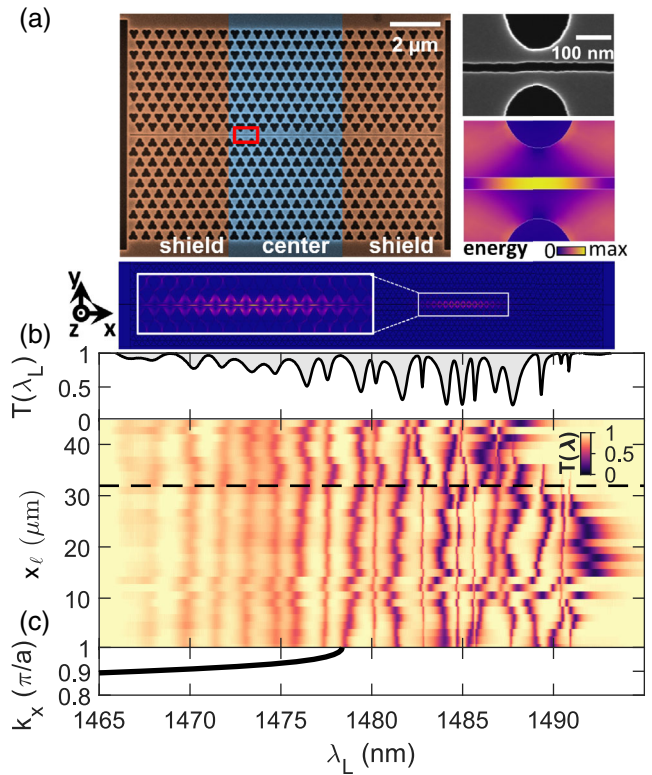


FIG. 2. (a) False-color SEM image of the shamrock optomechanical cavity waveguide formed by two PnC waveguides of mirror symmetry separated by an air slot. Enlarged SEM image of the latter (top right). Simulated electromagnetic energy confined within a perfect air slot (bottom right) and within a disordered slot (bottom). (b) Representative normalized optical transmission spectrum (top) taken by spatially probing at the position indicated by the dashed line in the map below. Spatially varying spectral map (bottom) in transmission (color scale) realized by moving the fiber loop along the waveguide. (c) Optical band structure showing the guided optical mode alongside the spectral map.

different fiber loop positions, denoted as  $x_\ell$ , along the waveguide axis. Spectra are acquired in steps of  $\sim 2 \mu\text{m}$  with  $x_\ell = 0$  and  $x_\ell = 75 \mu\text{m}$  denoting the two bounds of the central region. The resulting spatially varying spectral map is shown in Fig. 2(b), (bottom). The black dotted line indicates the position where the representative transmission spectrum is taken. At shorter wavelengths, periodic dips in transmission are observed which are extended Fabry-Pérot modes spanning the entire center region. While designed for the acoustic modes, the shield regions play an analogous role for the optics, creating a cavity waveguide for the slot-guided optical mode. At higher wavelengths the spectral location of the modes is less regular and the modes are spatially localized to specific sections of the waveguide in a manner akin to Anderson localization [35,39]. This results from localization of the light field due to multiple scattering off nanoscale fabrication imperfections resulting from etching at the silicon-air interface [SEM inset of the slot in Fig. 2(a)] [40]. This localization occurs where the

slot-guided light is slowed down [see slot-mode dispersion of the central region Fig. 2(c)] where the band flattens near the Brillouin zone edge. In this regime, light-matter interactions are enhanced and the system becomes increasingly sensitive to any nanoscale imperfections leading to optical mode volumes that decrease with increasing group index [41]. Consequently, these are the optical modes that are primarily of interest in this Letter. These modes are unavoidable when in the slow light regime. Above approximately  $\lambda = 1488$  nm the cutoff of the guided mode is reached and near-unity transmission is observed.

While exploiting fabrication imperfections could be considered a hindrance due to a lack of reproducibility, it is also advantageous as translational invariance of the elastic parameters is broken only at the level of roughness, leaving the acoustic Fabry-Perot modes largely unaffected due to the orders of magnitude difference in length scale. Exploitation of these imperfections allows for localization of the optical field without any deliberate adiabatic tuning of the geometry. The localized optical modes supported by this structure have moderate room-temperature  $Q$  factors below  $2 \times 10^4$ , much smaller than other optical cavities used for cavity optomechanics, including those that incorporate localized modes [35,42–44]. Nonetheless, when driving these localized optical modes, strong field confinement in the slot leads to considerable optomechanical coupling to the GHz acoustic modes, enabling their use as transducers of mechanical motion (see Supplemental Material [30] for schematic illustration summarizing the design's underlying physics).

We first obtain mechanical spectra via Brillouin light spectroscopy (BLS), where nonresonant light is focused onto the waveguide center and nonlinearly scattered by thermally activated acoustic phonons [Fig. 3(a)]. From BLS, the mechanical band gap spans 4.7 to 7.3 GHz with the phononic waveguide at 6.8 GHz (see Supplemental Material [30] with Refs. [27,32,45]). We further characterize the mechanical spectrum of the cavity waveguides with a fiber loop by measuring the optomechanically induced transmittance fluctuations of a monochromatic light source driving the localized optical cavities (see Supplemental Material [30] for experimental setup).

Figure 3(b) shows the rf spectrum detected with an electronic spectrum analyzer when a localized mode with central wavelength  $\lambda_L = 1484.5$  nm is driven with a blue-detuned laser. The signal-to-noise ratio is calculated from the power spectral density by normalizing to the noise level measured when the laser is off. The inset in Fig. 3(b) shows an enlargement around 6.76 GHz which, unlike the BLS spectrum, shows overlapping lines corresponding to different mechanical modes supported by the waveguide over a bandwidth of  $\approx 110$  MHz. These are roughly equispaced in frequency, and correspond to acoustic Fabry-Pérot modes such as those in Fig. 1(e). This bandwidth is smaller than the frequency span of the guided mode, indicating that the

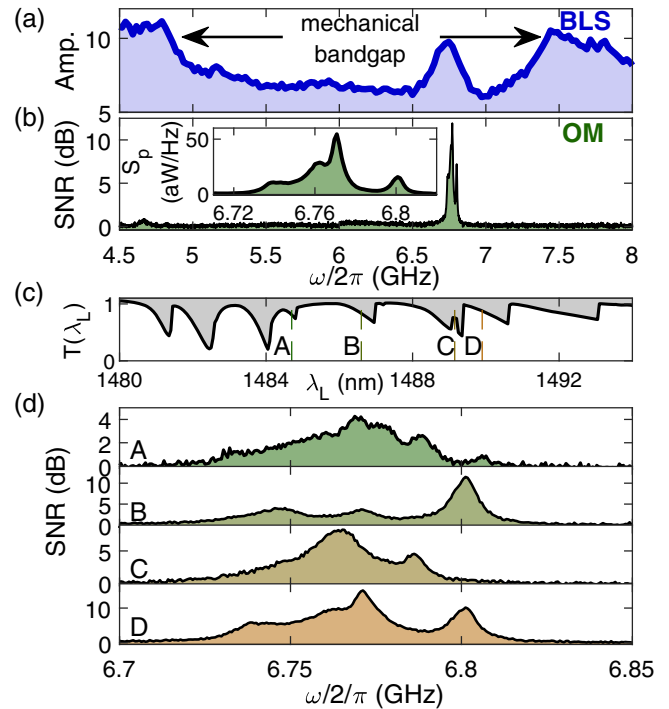


FIG. 3. (a) BLS spectroscopy measurement where a GHz mode is observed within the mechanical band gap. (b) The same mode is probed with the tapered fiber loop. Inset: magnified spectrum of this mode, allowing for the different peaks to be more clearly observed. (c) Normalized optical transmission spectrum showing localized optical-modes. (d) Mechanical spectra resulting from driving the optical modes indicated by dashed lines in (c).

optomechanical couplings  $g_0$  to the driven optical mode are too low in many cases. This is further supported by the relative intensities among the transduced peaks and through Figs. 3(c) and 3(d), which, respectively, show the optical transmission spectrum and the associated mechanical rf transduction spectra when four of the localized modes are driven [dashed lines in Fig. 3(c)].

The localized nature of the optical modes is revealed by both a strong thermo-optic nonlinearity resulting in a significant redshift [46,47] and in sawtooth-shaped line shapes [Fig. 3(c)], and by a strong optomechanical transduction. Driving optical modes below 1484 nm (Fabry-Pérot regime), no mechanical modes are observed above the noise floor. The transduction intensity generally increases when the laser drives an optical mode at longer wavelengths, due to reduced mode volumes, a higher  $Q$  factor of localized optical modes near the band cutoff, and stronger optomechanical coupling strengths [48]. Comparing spectra in Fig. 3(d), some of the observed mechanical peaks may appear in more than one spectrum or not at all due to a different transduction strength dependent on the driven optical mode. Similar results were obtained for cavities of varying lengths (see Supplemental Material [30]).

The strong confinement of the optical field in the air-slot and of the mechanical displacement to the waveguide

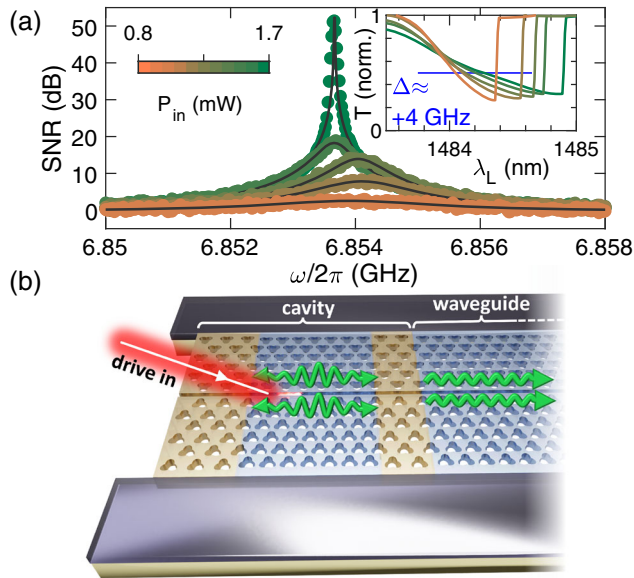


FIG. 4. (a) rf spectrum of the transmitted light showing optomechanical SSO, when the input power (color scale) increases. Inset: driven optical mode exhibiting a greater thermo-optic shift with increasing power. (b) Schematic illustration of a “phononic laser,” where acoustic waves (green arrows) are generated in the cavity which is side coupled to a waveguide.

region enables dynamical back-action and subsequent optomechanical SSO, indicated by the shifting, narrowing, and increase in amplitude of the mechanical peak with increasing laser power [Fig. 4(a)]. This occurs despite the relatively low values of the measured optical  $Q$  factor. The color scale indicates the input laser power and the inset shows the transmittance across the optical resonance as the laser power is varied, with high powers leading to a greater thermo-optic shift. The transduced spectra for each power are acquired at a fixed coupling fraction (blue line in inset), approximately corresponding to an effective detuning  $\Delta/2\pi = +4$  GHz. Even for relatively low input optical powers of  $\sim 1.6$  mW, high amplitude optomechanical SSO in the GHz is observed, yielding up to 50 dB amplification relative to the thermal regime. The transition from incoherent thermal motion to coherent optomechanical self-sustained oscillations is also indicated by the characteristic phase noise figure of the oscillator (see Supplemental Material [30]). Depending on the driven optical mode, different Fabry-Pérot acoustic modes [Fig. 3(d)] can be made to lase. For the particular optical and mechanical mode of Fig. 4(a), we extract an optomechanical coupling strength,  $g_0/2\pi$ , of 135 kHz from a linear fit of the mechanical linewidth versus input optical power [49] (see Supplemental Material [30]). This assumes optomechanical damping is the only source of linewidth narrowing, confirmed by calibration of the  $g_0/2\pi$  using an electro-optic phase modulator [50] (see Supplemental Material [30]), which further indicates the localized nature of the optical modes. The fit also returns a mechanical quality factor

$Q_m \sim 1176$  at zero input power, which is comparable with values found in similar systems at room temperature [14,32,51].

Here, we presented a 2D suspended silicon PnC waveguide sustaining a single acoustic band near 7 GHz within a 2.3 GHz-wide mechanical band gap, confirmed with BLS spectroscopy. To enable the generation of coherent acoustic phonons propagating along this waveguide mode, the structure was transformed into an efficient optomechanical waveguide by mirroring the PnC and leaving an air slot in the middle. This results in a slot photonic-crystal waveguide supporting a slot-guided optical mode at telecom wavelengths. We then exploited localized optical modes to couple to the original phononic waveguides on each side of the slot.

The optomechanical coupling strengths achieved are sufficient to enable coherent phonon generation at relatively low input powers directly within the waveguide. This is beneficial compared to previously employed optomechanical generation schemes that use a carefully engineered optomechanical cavity at the edge of the phononic waveguide of interest. This concept is schematically illustrated in Fig. 4(b) for the structure presented here. The generation bandwidth is not limited to the linewidth of a single mechanical cavity mode but to multiple mechanical modes which can be selectively driven using specific localized optical modes and then coupled into a perfectly mode-matched semi-infinite waveguide.

We acknowledge the support from the project LEIT funded by the European Research Council, H2020 Grant Agreement No. 885689. ICN2 is supported by the Severo Ochoa program from the Spanish Research Agency (AEI, Grant No. SEV-2017-0706) and by the CERCA Programme/Generalitat de Catalunya. R. C. N. acknowledges funding from the EU-H2020 research and innovation programme under the Marie Skłodowska Curie Individual Fellowship (Grant No. 897148). O. F. is supported by a BIST PhD fellowship under the Marie Skłodowska Curie Grant Agreement (No. 754558). M. A. and S. S. gratefully acknowledge funding from the Villum Foundation Young Investigator Program (Grant No. 13170), the Danish National Research Foundation (Grant No. DNRF147—NanoPhoton), Innovation Fund Denmark (Grant No. 0175-00022—NEXUS), and Independent Research Fund Denmark (Grant No. 0135-00315—VAFL).

\*These authors contributed equally to this work.

†Corresponding author.

ryan.ng@icn2.cat

‡Corresponding author.

david.garcia@icn2.cat

- [1] L. Wang and B. Li, *Phys. Rev. Lett.* **99**, 177208 (2007).
- [2] N. Li, J. Ren, L. Wang, G. Zhang, P. Hänggi, and B. Li, *Rev. Mod. Phys.* **84**, 1045 (2012).

- [3] S. R. Sklan, *AIP Adv.* **5**, 053302 (2015).
- [4] R. C. Ng, A. El Sachat, F. Cespedes, M. Poblet, G. Madiot, J. Jaramillo-Fernandez, O. Florez, P. Xiao, M. Sledzinska, C. M. Sotomayor-Torres, and E. Chavez-Angel, *Nanoscale* **14**, 13428 (2022).
- [5] A. Zivari, N. Fiaschi, R. Burgwal, E. Verhagen, R. Stockill, and S. Gröblacher, *Sci. Adv.* **8**, eadd2811 (2022).
- [6] D. Hatanaka, I. Mahboob, K. Onomitsu, and H. Yamaguchi, *Nat. Nanotechnol.* **9**, 520 (2014).
- [7] R. Van Laer, B. Kuyken, D. Van Thourhout, and R. Baets, *Nat. Photonics* **9**, 199 (2015).
- [8] W. Fu, Z. Shen, Y. Xu, C.-L. Zou, R. Cheng, X. Han, and H. X. Tang, *Nat. Commun.* **10**, 2743 (2019).
- [9] M. Su, R. Olsson III, Z. Leseman, and I. El-Kady, *Appl. Phys. Lett.* **96**, 053111 (2010).
- [10] Y. Soliman, M. Su, Z. Leseman, C. Reinke, I. El-Kady, and R. Olsson III, *Appl. Phys. Lett.* **97**, 193502 (2010).
- [11] R. Pourabolghasem, R. Dehghannasiri, A. A. Eftekhar, and A. Adibi, *Phys. Rev. Appl.* **9**, 014013 (2018).
- [12] R. Dehghannasiri, A. A. Eftekhar, and A. Adibi, *Phys. Rev. Appl.* **10**, 064019 (2018).
- [13] O. Florez, G. Arregui, M. Albrechtsen, R. C. Ng, J. Gomis-Bresco, S. Stobbe, C. M. Sotomayor-Torres, and P. D. García, *Nat. Nanotechnol.* **17**, 947 (2022).
- [14] K. C. Bahram, M. I. Davanço, J. D. Song, and K. Srinivasan, *Nat. Photonics* **10**, 346 (2016).
- [15] L. Shao, S. Maity, L. Zheng, L. Wu, A. Shams-Ansari, Y.-I. Sohn, E. Puma, M. N. Gadalla, M. Zhang, C. Wang, E. Hu, K. Lai, and M. Lončar, *Phys. Rev. Appl.* **12**, 014022 (2019).
- [16] A. Korovin, Y. Pennec, M. Stocchi, D. Mencarelli, L. Pierantoni, T. Makkonen, J. Ahopelto, and B. Djafari-Rouhani, *J. Phys. D* **52**, 32LT01 (2019).
- [17] A. S. Kuznetsov, D. H. O. Machado, K. Biermann, and P. V. Santos, *Phys. Rev. X* **11**, 021020 (2021).
- [18] Y. D. Dahmani, C. J. Sarabalis, W. Jiang, F. M. Mayor, and A. H. Safavi-Naeini, *Phys. Rev. Appl.* **13**, 024069 (2020).
- [19] F. M. Mayor, W. Jiang, C. J. Sarabalis, T. P. McKenna, J. D. Witmer, and A. H. Safavi-Naeini, *Phys. Rev. Appl.* **15**, 014039 (2021).
- [20] D. Navarro-Urrios, M. F. Colombano, G. Arregui, G. Madiot, A. Pitanti, A. Griol, T. Makkonen, J. Ahopelto, C. M. Sotomayor-Torres, and A. Martinez, *ACS Photonics* **9**, 413 (2022).
- [21] L. Shao, D. Zhu, M. Colangelo, D. Lee, N. Sinclair, Y. Hu, P. T. Rakich, K. Lai, K. K. Berggren, and M. Lončar, *Nat. Electron. Rev.* **5**, 348 (2022).
- [22] M. J. Burek, J. D. Cohen, S. M. Meenehan, N. El-Sawah, C. Chia, T. Ruelle, S. Meesala, J. Rochman, H. A. Atikian, M. Markham, D. J. Twitchen, M. D. Lukin, O. Painter, and M. Lončar, *Optica* **3**, 1404 (2016).
- [23] D. Navarro-Urrios, N. E. Capuj, J. Gomis-Bresco, F. Alzina, A. Pitanti, A. Griol, A. Martínez, and C. M. Sotomayor-Torres, *Sci. Rep.* **5**, 15733 (2015).
- [24] I. Ghorbel, F. Swiadek, R. Zhu, D. Dolfi, G. Lehoucq, A. Martin, G. Moille, L. Morvan, R. Braive, S. Combré *et al.*, *APL Photonics* **4**, 116103 (2019).
- [25] W. Jiang, R. N. Patel, F. M. Mayor, T. P. McKenna, P. Arrangoiz-Arriola, C. J. Sarabalis, J. D. Witmer, R. V. Laer, and A. H. Safavi-Naeini, *Optica* **6**, 845 (2019).
- [26] L. Mercadé, K. Pelka, R. Burgwal, A. Xuereb, A. Martínez, and E. Verhagen, *Phys. Rev. Lett.* **127**, 073601 (2021).
- [27] R. N. Patel, Z. Wang, W. Jiang, C. J. Sarabalis, J. T. Hill, and A. H. Safavi-Naeini, *Phys. Rev. Lett.* **121**, 040501 (2018).
- [28] J. Guo, R. Norte, and S. Gröblacher, *Phys. Rev. Lett.* **123**, 223602 (2019).
- [29] F. Wen, S. David, X. Checoury, M. E. Kurdi, and P. Boucaud, *Opt. Express* **16**, 12278 (2008).
- [30] See Supplemental Material at <http://link.aps.org/supplemental/10.1103/PhysRevLett.130.106903> for additional BLS and optomechanical measurements, along with numerical simulations.
- [31] J. Gomis-Bresco, D. Navarro-Urrios, M. Oudich, S. El-Jallal, A. Griol, D. Puerto, E. Chavez, Y. Pennec, B. Djafari-Rouhani, F. Alzina, A. Martínez, and C. M. Sotomayor-Torres, *Nat. Commun.* **5**, 4452 (2014).
- [32] K. Fang, M. H. Matheny, X. Luan, and O. Painter, *Nat. Photonics* **10**, 489 (2016).
- [33] P. D. García, R. Bericat-Vadell, G. Arregui, D. Navarro-Urrios, M. Colombano, F. Alzina, and C. M. Sotomayor-Torres, *Phys. Rev. B* **95**, 115129 (2017).
- [34] G. Arregui, D. Navarro-Urrios, N. Kehagias, C. M. Sotomayor Torres, and P. D. García, *Phys. Rev. B* **98**, 180202(R) (2018).
- [35] G. Arregui, R. C. Ng, M. Albrechtsen, S. Stobbe, C. M. Sotomayor-Torres, and P. D. García, *Phys. Rev. Lett.* **130**, 043802 (2023).
- [36] V. T. H. Nguyen, C. Silvestre, P. Shi, R. Cork, F. Jensen, J. Hubner, K. Ma, P. Leussink, M. de Boer, and H. Jansen, *ECS J. Solid State Sci. Technol.* **9**, 024002 (2020).
- [37] M. Albrechtsen, B. Vosoughi Lahijani, R. E. Christiansen, V. T. H. Nguyen, L. N. Casses, S. E. Hansen, N. Stenger, O. Sigmund, H. Jansen, J. Mørk, and S. Stobbe, *Nat. Commun.* **13**, 6281 (2022).
- [38] V. T. Hoang Nguyen, F. Jensen, J. Hübner, E. Shkondin, R. Cork, K. Ma, P. Leussink, W. De Malsche, and H. Jansen, *J. Vac. Sci. Technol. B* **39**, 032201 (2021).
- [39] P. W. Anderson, *Phys. Rev.* **109**, 1492 (1958).
- [40] N. Le Thomas, H. Zhang, J. Jágerská, V. Zabelin, R. Houdré, I. Sagnes, and A. Talneau, *Phys. Rev. B* **80**, 125332 (2009).
- [41] L. Sapienza, H. Thyrrerstrup, S. Stobbe, P. D. Garcia, S. Smolka, and P. Lodahl, in *Conference on Lasers and Electro-Optics 2010* (Optical Society of America, New York, 2010), p. QPDA7.
- [42] M. Eichenfield, J. Chan, R. M. Camacho, K. J. Vahala, and O. Painter, *Nature (London)* **462**, 78 (2009).
- [43] M. Mitchell, A. C. Hryciw, and P. E. Barclay, *Appl. Phys. Lett.* **104**, 141104 (2014).
- [44] J. Topolancik, F. Vollmer, and B. Ilic, *Appl. Phys. Lett.* **91**, 201102 (2007).
- [45] Q. Liu, H. Li, and M. Li, *Optica* **6**, 778 (2019).
- [46] D. Navarro-Urrios, J. Gomis-Bresco, N. E. Capuj, F. Alzina, A. Griol, D. Puerto, A. Martínez, and C. M. Sotomayor-Torres, *J. Appl. Phys.* **116**, 093506 (2014).
- [47] J. Maire, G. Arregui, N. E. Capuj, M. F. Colombano, A. Griol, A. Martinez, C. M. Sotomayor-Torres, and D. Navarro-Urrios, *APL Photonics* **3**, 126102 (2018).

- [48] M. G. Scullion, Y. Arita, T. F. Krauss, and K. Dholakia, *Optica* **2**, 816 (2015).
- [49] M. Aspelmeyer, T. J. Kippenberg, and F. Marquardt, *Rev. Mod. Phys.* **86**, 1391 (2014).
- [50] M. Gorodetsky, A. Schliesser, G. Anetsberger, S. Deleglise, and T. Kippenberg, *Opt. Express* **18**, 23236 (2010).
- [51] H. Ren, T. Shah, H. Pfeifer, C. Brendel, V. Peano, F. Marquardt, and O. Painter, *Nat. Commun.* **13**, 3476 (2022).